Linköping University Post Print

Colour moiré interferometry for physical sensing using a standard web camera

Stephen Macken and Daniel Filippini

N.B.: When citing this work, cite the original article.

Colour Moiré Interferometry for Physical Sensing Using A Standard Web-Camera

S. Macken[1] and D. Filippini[1].

[1] IFM, Department of Applied Physics, Linköpings University, 581 83 Linköping, Sweden.

Email: stema@ifm.liu.se

Abstract:

Digital moiré patterns are an effect seen in digital pictures when a high contrast periodic object being imaged interferes with the periodic image detector in the camera. This is often an undesired effect, which is usually removed through various filtering processes. However in this work we demonstrate the ability to use a deliberately created Moiré pattern to measure the physical distance of an object from a web-camera with a resolution of 131 μm. This measurement principle is then adapted to measure weight as a ubiquitous scale with a resolution of 240 μg.

Introduction:

Modern consumer electronic devices constitute a pervasive infrastructure capable of different functions, from those that they are originally conceived for. They are sophisticated equipment, but at the same time familiar to users and designed to be operated by the general consumer. Additionally, there is an autonomous and continuous improvement of their capabilities and a frequent renewal by newer models. All these characteristics make certain consumer electronic devices attractive as platforms for distributed chemical sensing or diagnostic uses. One instrumentation strategy is to co-opt the optical capabilities of devices such as flat bed scanners [i,ii], CD players [iii,iv], radio frequency identification (RFID) tags [v], computer screens operating as light sources in combination with web cameras as detectors (computer screen photo assisted technique, CSPT [vi, vii, viii]) and mobile phones [ix], and turn them into chemical sensing terminals by adding a (disposable) sensing element.

CSPT in particular has been demonstrated as a versatile method supporting multiple detection principles including excitation emission matrix fingerprinting [x], ellipsometry [xi] and surface plasmon resonance (SPR) [xii]. The use of optical microstructures for spectral fingerprinting [xiii,xiv] has shown the generation of red, green and blue interference patterns, which have been exploited for the acquisition of Bayer [xv] images that avoid the use of device specific drivers to prevent demosaicing [xiv, xvi]. A missing demonstration of CSPT is its extension to physical measures. Within the tenets of the ubiquitous instrumentation concept, we aim at demonstrating a scale for CSPT by adding a passive sensing element and using the inherent capabilities of the platform to do the rest.

Moiré interferometry is a well-established and widespread technology in strain measurement [xvii, xviii, xix]. Examples of applications include pressure, displacement, thickness, thermal deformation and position measurements [xx, xxi, xxii, xxiii, xxiv, xxv]. In these applications the camera and setup are selected around the target experiment, without any intention of making the systems ubiquitous or able to operate on generic platforms. On the other hand, a technique such as CSPT scavenges the remnant capabilities of familiar devices making it possible to perform diverse experiments while coexisting on the same platform.

In this work we demonstrate, model, and characterize the generation of colour Moiré patterns using regular web cameras for the accurate monitoring of displacement and its application as a ubiquitous scale.

Materials and Methods:

As defined in [xxvi] the moiré effect seen in digital photography is a result of spatial interference. When imaging a high contrast periodic object with a digital camera, like the Cr mask of figure 1 (b), spatial interference occurs between this pattern and the also periodic image detector array with its Bayer filter. In our setup this effect is taken advantage of in order to monitor the distance between the camera and a periodic pattern. By then introducing a spring in the support structure of the periodic pattern it is possible to transduce displacement into a weight measurement.
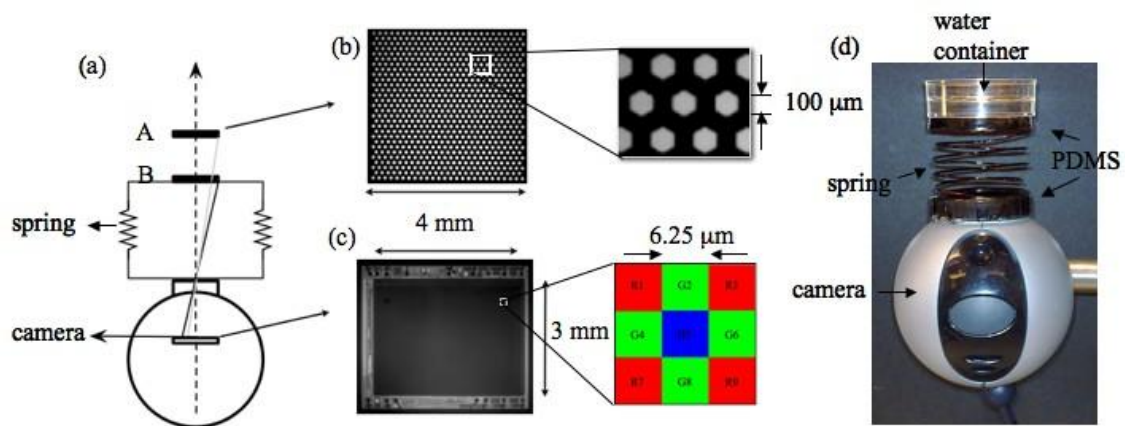

Figure 1: a) Setup for moiré interferometric measurement with a spring or vertical translator. Position A is the position of the mask before displacement and B is its position after displacement. b) Cr patterned mask with 100 μm hexagonal holes. c) Image detector of Logitech Quickcam Pro and numbered detail of Bayer filter, where R1, R3, R7 and R9 are red channel pixels. G2, G4, G6 and G8 are green channel pixels and B5 is a blue channel pixel. For coloured version please refer to the online paper. d) Setup showing the PDMS support structure and spring used to measure weight displacement via moiré pattern evaluation via the web-camera. A computer screen was then mounted above the setup to provide the stable illuminating source (not pictured here).

Figure 1 (a), displays a Logitech Quickcam Pro™ and a micro-patterned glass substrate in an arrangement that produces intense moiré patterns in the acquired images. Illumination was provided by a Philips 170/s2 LCD screen operating in normal conditions of intensity and contrast and at 1280×1024 pixels 32 bits colour resolution at a standard refresh frequency of 60 Hz, displaying a blank white area, giving a low intensity, easily controlled, light source. This source was a convenient choice for controlled lab conditions, but this technique operates under ambient light conditions as well.

The micro-patterned Cr mask (fig. 1 (b)) was created by using a Menzel-Glaser microscope glass slide, first coated in 150 nm of Cr and then spun coated with a layer of S1818 photoresist. After exposing this to patterned UV light, using photolithographic procedures [xxvii], a pattern in the S1818 was developed and the Cr surface was chemically etched leaving a patterned Cr film on top of a transparent substrate. This periodic pattern of holes masks the backside illumination and produce 100 μm wide, 70 μm spaced, hexagonal light spots (fig. 1(b)).

The image detector used in this work is a Logitech Quickcam Pro with a VGA (640 x 480 pixels) CCD detector with 24 bits colour resolution. Figure 1 (c) shows the CCD of the Logitech camera. Each pixel is 6.25 x 6.25 μm in size and is coated by a colour filter. These filters are red, green or blue and form a checker like pattern (fig. 1 (c)), called a Bayer filter.

There are twice as many green as red and blue areas in order to simulate the sensitivity of the human eye. The colour value of each pixel in the final image is then the composed value from the nearest neighbours, a process called demosaicing [xvi].

For the resolution of the detector with its' particular lens characteristics and the chosen measuring distances a moiré pattern is efficiently created with the mask layout used here. The main aberrations to expect in these systems are vignetting and barrel distortion, which in our case are minimized by using only the central part of the captured image. The target area is just 4 x 4 mm at a distance of over 2 cm, which is why a large zoom percentage is used c.f. next paragraph. For high-end cameras or mobile phone cameras the key variables are the same, the pixel pitch and size and the minimum focal distances, which will determine the most adequate mask layout for a compact arrangement. In our experiments we kept the mask and the imager parallel, which was necessary to produce results that we could explain with the considered model; however, the measuring principle should be robust to parallelism if such alignment is kept for different distances. A model considering a variable pitch should be considered for the generation of each pattern, in such conditions.

This camera is a simple consumer web-camera with no functionality for raw image data access. The exact process steps of image acquisition are also not available to the general public. However, digital image capturing must still contain basic steps, which we replicate in our modelling later on. One step in particular, though, has many methods of application i.e. demosaizing [xvi], where the intensity information from the filtered pixels are constructed into the final digital image. For this work we therefore chose one method that is often used for simple image capturing equipment that also provided us with similar results to the recorded images using the Logitech web-camera.

To accurately infer a position shift from the interference pattern the setup had to be calibrated. Accordingly the mask (fig. 1 (b)) was mounted on a Narishige ltd. MM-87 motor-drive manipulator, which enabled the precise displacement of the Z coordinate, where Z is the distance between the camera lens ring and the mask. Starting at 2.5 cm the grid receded from the camera in steps of approx. 90 μm up to a distance of 3.5 cm. At each step a picture was taken with the web-camera using the following settings: brightness 40%, contrast 50%, gain 0%, saturation 100%, shutter speed 1/100, white balance set to daylight and the zoom at 220%, resulting in a total of 111 pictures. The camera used in this paper has a manual focus ring, which means that after the grid had been displaced by a certain amount the camera required re-focussing. This occurred at three points: Z= 28 mm, 31 mm and at 32.5 mm.

To demonstrate the measurement of weight using this system the motor-driven manipulator was replaced by a Cu wire spring of diameter 0.71 mm. The spring was held in place using two Dow Corning Sylgard 184 PDMS (polydimethylsiloxane) moulded parts. The base PDMS, which was on top of the camera, was moulded to the shape of the focus ring and the top PDMS, which formed a stand for the glass substrate, was circular with a hole in the centre to allow clear viewing of the grid pattern.

The spring was glued between these two parts using PDMS (all PDMS parts were made with a base/curing agent ratio of 10:1). The spring and PDMS were then spray painted black to ensure that only light passing through the Cr patterned glass substrate entered the camera. A transparent plastic container was placed atop the patterned glass substrate and, for stability, was preloaded with 3 mg of water, figure 1 (d). Pictures were then taken with the camera as 100 μg of water were added one at a time to a total weight of 5 mg. The camera settings used in these measurements were the same as before except for the shutter speed, which was 1/50 s.

Model:

The following model describes the formation of spatial interference patterns between two periodic structures defined by a periodic array of bright regions (the mask) and a periodic array

of colour filters (camera detector), for different scales of the mask patterns associated to the distance between the mask and the camera lens. A model replicating this process of image capturing was created, in Matlab, to simulate and predict observed results. Figure 2 shows the four-step process involved in the simulation of the interference patterns.
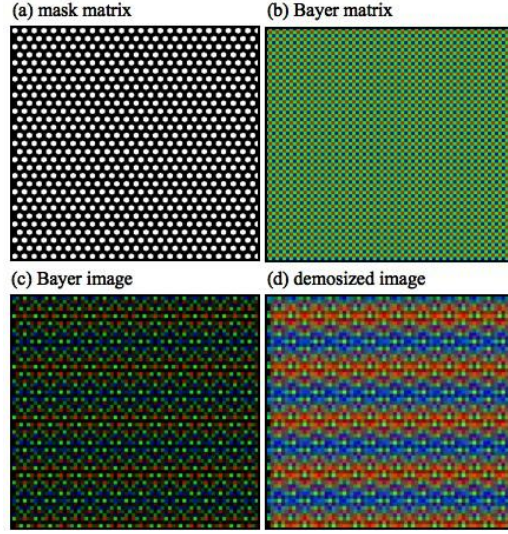

Figure 2: a) Matrix representation of Cr patterned hexagonal holes. b) Bayer matrix of red, green and blue pixels. c) Bayer image prior to demosizing, showing alternating blue and red lines. d) Final image demosized through bi-linear interpolation, showing alternating blue and red stripes. For coloured version please refer to the online paper.

The first step was the generation of an illuminating pattern equivalent to that of the Cr mask. This was achieved by defining a matrix with ones and zeros, with the ones representing the hexagonal holes of the Cr pattern when light is shining through. The size of the matrix used for one hexagonal pattern was 71 x 65 creating a total matrix size of 2800 x 2960. However for simplicity a single hexagonal hole geometry can be represented by,

$$h_c = \begin{vmatrix} 0 & 0 & 0 & 1 & 0 & 0 & 0 \\ 0 & 1 & 1 & 1 & 1 & 1 & 0 \\ 1 & 1 & 1 & 1 & 1 & 1 & 1 \\ 1 & 1 & 1 & 1 & 1 & 1 & 1 \\ 1 & 1 & 1 & 1 & 1 & 1 & 1 \\ 0 & 1 & 1 & 1 & 1 & 1 & 0 \\ 0 & 0 & 0 & 1 & 0 & 0 & 0 \end{vmatrix} \quad \text{with } h_m \text{ x } h_n \text{ elements.} \tag{1}$$

the coordination and pitch between elements can be defined by

$$M_{h_c} = h_c \cdot \delta\left(C_x, C_y\right) \tag{2}$$

where

$$\delta \text{ is } \begin{cases} 1 & \forall\left(C_x, C_y\right) \\ 0 & otherwise \end{cases} \tag{3}$$

and the coordinates of each pillar are defined by

$$C_y = C_{0y} + d_y \cdot \left(n_y - 1\right) \tag{4}$$

$$C_x = \begin{cases} C_{0x} + d_x \cdot (n_x - 1) & \forall \quad n_y \quad odd \\ C_{0x} + d_x \cdot (n_x - 1) + \dfrac{d_x}{2}, \forall & n_y \quad even \end{cases} \tag{5}$$

with

$$d_x > h_n \tag{6}$$

and

$$d_y > h_m \tag{7}$$

being the pitch that determines the layout, and n_x and n_y are the indexes of each hole in the pattern matrix.

Since we produce a colour simulation of the pattern this corresponds to a 3D matrix where the third dimension is interpreted as the intensity value of the red, green and blue layers respectively. Therefore the matrix of figure 2 (a) is made up of three equal layers of ones and zeros, simulating white light as a computer screen creates such a coloured light through equal portions of red, green and blue illumination.

The illumination matrix is thus,

$$\begin{cases} M_{I_{i,j,k=1}} = M_{h_c} & red \quad channel \\ M_{I_{i,j,k=2}} = M_{h_c} & green \quad channel \\ M_{I_{i,j,k=3}} = M_{h_c} & blue \quad channel \end{cases} \tag{8}$$

The camera detector is another cell array but with a superimposed Bayer filter, (fig. 2 (b)). Depending on the size of the illuminating pattern and the distance to the camera, different proportions of the illuminating patterns will be projected onto this detector. Thus the size of the detector cell under each camera filter must vary to accurately simulate the distance from the patterned source,

$$b_{\alpha \cdot h_m, \alpha \cdot h_n} = 1 \tag{9}$$

with α as the parameter determining the relative sizes and pitches in respect to the illuminating pattern size, which in our case was 0.458 of the grid pattern hole size at 25 mm and 0.583 at 35 mm. This means that between 45 % and 58 % of the total light intensity coming from a hexagonal 100 μm shape will reach a single pixel. Since the matrices simulating these aspects contain integer number of elements, increasing the number of elements in the simulation allowed for a better approximation of the given proportions.

In order to create the Bayer checker pattern in fig. 2 (b) we write for the three filter channels,

$$\begin{cases} M_{B_{i,j,k=1}} = b \cdot \delta(r_x, r_y) \\ r_x = 2 \cdot \alpha \cdot h_n \cdot (p_x - 1) & red \; channel \\ r_y = 2 \cdot \alpha \cdot h_m \cdot (p_y - 1) \end{cases} \tag{10}$$

$$\begin{cases} M_{B_{i,j,k=2}} = b \cdot \delta(b_x, b_y) \\ b_x = \alpha \cdot h_n + 2 \cdot \alpha \cdot h_n \cdot (p_x - 1) & blue \; channel \\ b_y = \alpha \cdot h_m + 2 \cdot \alpha \cdot h_m \cdot (p_y - 1) \end{cases} \tag{11}$$

$$\begin{cases} M_{B_{i,j,k=3}} = b \cdot \delta\left(\left(g_{x_1}, g_{y_1}\right) + \left(g_{x_2}, g_{y_2}\right)\right) \\ g_{x_1} = 2 \cdot \alpha \cdot h_n \cdot \left(p_x - 1\right) \\ g_{y_1} = \alpha \cdot h_m \cdot \left(p_x - 1\right) \\ g_{x_2} = \alpha \cdot h_n \cdot \left(p_x - 1\right) \\ g_{x_2} = 2 \cdot \alpha \cdot h_m \cdot \left(p_x - 1\right) \end{cases} \qquad green\ channel \qquad (12)$$

with p_x and p_y representing the index of each cell in the detector. For an illuminating pattern with N_x and N_y holes the total number of elements in M_I is

$$N_x \cdot d_x + h_n, \qquad N_y \cdot d_y + h_m \qquad (13)$$

and the total number of detector cells P_x and P_y should be

$$P_x = \frac{N_x \cdot d_x}{\alpha \cdot h_n} \qquad and \qquad P_y = \frac{N_y \cdot d_y}{\alpha \cdot h_m} \qquad (14)$$

Accordingly, the Bayer image of the patterned source, (fig. 2 (c)), is simply the product of the array elements:

$$B_{i,j,k} = M_{I_{i,j,k}} \times M_{B_{i,j,k}} \qquad (15)$$

The final image rendered from the camera is the demosized version of B. Using a common processing technique [xxviii] a value for the one channel in the positions of the other channels pixels can be calculated, and considering the detail of the Bayer filter from figure 1 (c),

$$\begin{cases} R2 = (R1 + R3)/2 \\ R4 = (R1 + R7)2 & red \\ R5 = (R1 + R3 + R7 + R9)/4 \\ G5 = \left(G2 + G4 + G6 + G8\right)/4 & green \\ & blue: same\ as\ red \end{cases} \qquad (16)$$

the final result of fig. 2 (d) is produced.

The calibration measurement performed with the motor-driven manipulator covered a distance along Z of 1 cm ranging from 25 mm to 35 mm, so as mentioned before this covered an α range from 0.458 to 0.583. The model was validated along 11 points in this range.

Results and Discussion:

Visual comparison between the model and measured moiré patterns shows a very good agreement, figure 3. As the Cr mask moves further away from the camera the period of the moiré interference increases.
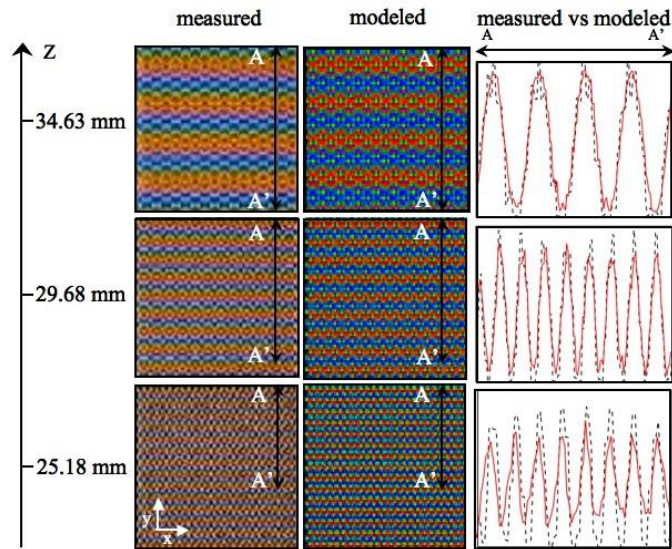
Figure 3: Column 1 and 2: Illustration of modelled moiré image compared to measured moiré image for the Z-distances, with alternating blue and red stripes. Column 3: Examples of the single line sinusoidal pixel intensity modulations of the measured moiré images (red/solid line) and model (black/dashed line) in the marked regions A – A'. These have been compensated for the phase difference between the model and measured pictures to illustrate their matching quality in ϕ. For coloured version please refer to the online paper.

For the coordination of the Cr mask layout (a closed packed 2D arrangement) the resulting moiré occurs on a preferential direction. Other mask layouts can create periodic patterns in both axes. The images have strong blue and red features, which essentially provide the same information, thus the evaluation of only one of these colours was necessary, and due to the periodic nature of the images we evaluated just the ½ period (henceforth called "ϕ") value for each picture along "y", for the full length of the picture, and taking the average value of the intensity along the x-direction. Thus, we use ϕ from the blue channel to monitor Z, (fig. 3 column 3).

The measured moiré images varied in size depending on Z, and in order to anchor the relationship with the modelled moiré images all measured images along A-A' are re-sampled to 1600 points, which also improves the accuracy in the determination of ϕ. After the final evaluation the ϕ values were then re-scaled back to the range measured in the images.
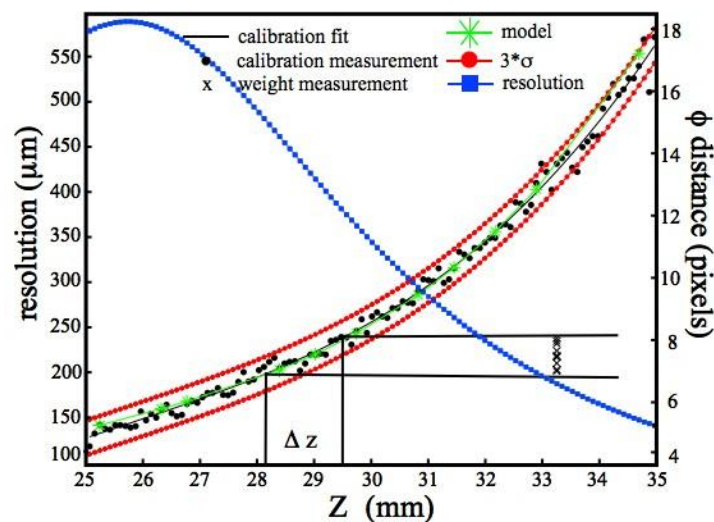

Figure 4: Graph of ϕ for the calibration (black dots and best-fit black solid line) and model (best-fit green star marked line) with 3 σ error lines (red circle marked lines). Weight measurements (x) calibrated to the best-fit line. The blue

line with square markers is the resolution of the system over the investigated range of distances. For coloured version please refer to the online paper.

Figure 4 shows the moiré response (ϕ) with Z in the studied range (25-35 mm), the best fitting to the experimental values (black line) and the modelled response (green line), which is within the 95 % confidence interval (red lines). Minor discrepancies with the experimental results can be attributed to refocusing during the measurement (that occurred at 32.5 mm) and the demosaicing method assumed for the model.

As can be observed in fig. 4 the response is not linear and accordingly the sensitivity varies along the Z range, with a maximum of 2.8×10^{-3} pixels / μm at 35 mm. The noise level (3σ) of a single experimental ϕ value evaluated over a collection of 10 acquisitions is, $\pm$ 0.37 pixels, however, the variability between different determinations, which in fact reflect the error of the manipulator used for the calibration, is about 3 times this value. Thus, considering the error of the moiré alone, the resolution varies between 570 μm to 130 μm between 25 and 35 mm respectively.

It has been shown elsewhere [xxix] that resolutions of fractions of microns are attainable with dedicated instruments. However, 130 μm resolution is still an interesting and useful performance considering the employed resources. In fact, if the size of an imaged object was used to evaluate Z instead of the moiré, using the same camera, the minimum detectable displacement of 1 pixel would correspond to 1.45 mm in Z or about 11 times poorer than our method.

One practical use of distance measurement with our system resolution can be simply for positioning or as demonstrated in this case, by transducing weight into displacement to create a simple scale. The transduction coefficient will depend on the used springs and the performance as a balance will certainly depend on the quality of the assembly.

Ten measurements were performed from 3.1 mg (position A fig. 1) to 4.1 mg (position B fig. 1) in 100 μg steps. Each weight produced a characteristic moiré pattern, which was evaluated through its' ϕ. The ϕ values of these 10 measurements are plotted in fig. 5 (x symbols). These weights correspond to a 1700 μm total displacement, a spring constant of 5.88×10^{-4} mg / μm, an average sensitivity of 1.54 pixels / mg and an average displacement resolution of 411 μm. For the same error considered in the displacement measurements, the resulting resolution is 240 μg.

The weights range of displacement is clearly outside the best sensitivity for the present arrangement (where a 130 μm could give a 77 μg resolution), and the quality of the construction, admits further improvement. However, a 240 μg resolution is already a useful performance. Further, tuning the Cr mask, and spring constant can certainly produce well-conditioned and compact scales for varied weight ranges.

In the present arrangement the substance to be weighed must be transparent. This tough is just a peculiarity of the present setup, rather than a fundamental limitation of the concept. Where for example using reflecting elements or changing the design of the supporting cup could solve this limitation. These and more are aspects that we will certainly try to incorporate in future developments, especially for targeting the implementation on mobile phones, which is the natural evolution of this technique towards ubiquity.

Conclusions:

Displacement measurement via moiré interference, with a resolution of 130 μm, was demonstrated on a CSPT platform using a regular web-camera as a detector. A working computer model of moiré pattern generation through spatial interference in the CSPT platform has been developed and validated providing the developer with a tool to optimize a grid/CCD

setup prior to experimentation. Finally a weight to displacement transduction demonstrated the feasibility of the CSPT system as a ubiquitous scale with a 240 μg resolution.

The results here show the feasibility to introduce physical sensing, by transducing an accurate displacement measurement, to the CSPT ubiquitous sensing platform, thus complementing this type instrumentation, which prior to this work has been exclusively used for chemical sensing experiments. Displacement measurements offer a generic principle to transduce diverse type of physical parameters, among them weight as shown here, but also flow, temperature and pressure are important candidates to complement ubiquitous chemical sensing experiments, which are compatible with the demonstrated concept.

References:

[i] Hruschka W. R., Massie D. R., Anderson J. D. 1983 *Computerized analysis of two-dimensional electrophoretograms*, Anal. Chem. **55** 2345-2348.

[ii] Rakow N. A., Suslick K. S. 2000 *A colorimetric sensor array for odour visualization*, Nature **406** 710-713.

[iii] Johnson R. D., Badr I. H., Barrett G., Lai S., Lu Y., Madou M. J., Bachas L. G. 2001 *Development of a fully integrated analysis system for ions based on ion-selective optodes and centrifugal microfluidics,* Anal. Chem. **73** 3940-3946.

[iv] Potyrailo R. A., Morris W. G., Leach A. M., Sivavec T. M., Wisnudel M. B., Boyette S. 2006 *Analog signal acquisition from computer optical disk drives for quantitative chemical sensing,* Anal. Chem. **78** 5893-5899.

[v] Potyrailo R. A., Morris W. G. 2007 *Multianalyte Chemical Identification and Quantitation Using a Single Radio Frequency Identification Sensor* Anal. Chem. **79** 45-51.

[vi] Filippini D., Alimelli A., DiNatale C., Paolesse R., D'Amico A., Lundström I. 2006 *Chemical sensing with familiar devices*, Angew. Chem. Int. Ed. **45** 3800–3803.

[vii] Alimelli A., Pennazza G., Santonico M., Paolesse R., Filippini D., D'Amico A., Lundström I. and Di Natale C. 2007 *Fish Freshness detection by a computer screen photo-assisted based gas sensor array*, Anal. Chim. Acta **58** 2320-328.

[viii] Suska A., Filippini D., Andersson T.P.M. and Lundström I. 2005 *Generation of biochemical response patterns of different substances using a whole cell assay with multiple signaling pathways* Biosens. Bioelect. **21** 727-734.

[ix] Breslauer DN, Maamari RN, Switz NA, Lam WA, Fletcher DA 2009 *Mobile Phone Based Clinical Microscopy for Global Health Applications*. PLoS ONE **4**(7): e6320. doi:10.1371/journal.pone.0006320.

[x] Gatto E., Malik M. A., Di Natale C., Paolesse R., D'Amico A., Lundström I., Filippini D. 2008 *Polychromatic Fingerprinting of Excitation Emission Matrices*, Chem. Eur. J. **14** 6057-6060.

[xi] Bakker J.W.P., Arwin H., Lundström I., Filippini D. 2006 *Computer screen photo-assisted offnull ellipsometry*, Appl. Optics **45** 7795-7799.

[xii] Filippini D., Winquist F., Lundström I. 2008 *Computer screen photo-excited surface plasmon resonance imaging*, Anal. Chim. Acta **635** 207-214.

[xiii] Macken S., Lundström I., Filippini D. 2006 *Optical properties of microstructures for computer screen photo-assisted experiments,* Appl. Phys. Lett. **89** 254104.

[xiv] Macken S., Di Natale C., Paolesse R., D' Amico A., Lundström I., Filippini D. 2009 *Towards integrated devices for computer screen photoassisted multi-parameter sensing,* Anal. Chim. Acta **632** 143-147.

[xv] Bayer B.E. *Color Imaging Array* U.S. Patent 3,971,065 July 20 1976.

[xvi] Kimmel R. *Demosaicing: Image Reconstruction from CCD Samples* 1999 IEEE Transactions on image processing **8** pp 1221-1228.

[xvii] Cordero R.R., Francois M., Lira I., Vial-Edwards C. 2005 *Whole-field analysis of uniaxial tensile tests by Moiré interferometry* Optics and Lasers in Engineering **43** 919–936.

[xviii] Huimin X., Fulong D., Dietz P., Schmidt A., Wei Z. 1999 *600°C creep analysis of metals using the Moiré interferometry method* Journal of Materials Processing Technology **88** 185 – 189.

[xix] Gungor S. 2002 *Residual stress measurements in fibre reinforced titanium alloy composites* Acta Materialia **50** 2053–2073.

[xx]A. P. Vafiadakis. 1967 *Two moiré instruments* J. Sci. Instrum. **44** 1008 – 1010.

[xxi] Tu T. and Boon Goh W. 2009 *Using CCD Moiré Pattern Analysis to Implement Pressure-Sensitive Touch Surfaces* CAIP LNCS **5702**, pp. 1228–1235.

[xxii] Ri S. and Muramatsu T. 2010 *A simple technique for measuring thickness distribution of transparent plates from a single image by using the sampling moiré method* Meas. Sci. Technol. **21** 025305.

[xxiii] Yamamoto Y., Morimoto Y. and Fujigaki M. 2007 *Two-directional phase-shifting moiré interferometry and its application to thermal deformation measurement of an electronic device* Meas. Sci. Technol. **18** 561.

[xxiv] V Gierie W., L Paterson R., H Brown W. and R Proffit W. 1998 *Accuracy of movement tracking with a miniaturized second-generation Moiré device* Physiol. Meas. **19** 383–392.

[xxv] Torroba R., Bolognini N., Tebaldi M., Tagliaferri A. 2002 *Positioning method based on digital moiré* Optics Communications **209** 1–6.

[xxvi] Rosenfeld A. and Kak A.C. *Digital Picture Processing* 1976 (New York: America, London: England) Academic Press 1st Ed. Ch. 4 pp 76-83.

[xxvii] Peterman M.C., Huie P., Bloom D.M., Fishman H.A. 2003 *Building thick photoresist structures from the bottom up* J. Micromech. Microeng. **13** 380–382.

[xxviii] Lukin A., Kubasov D. 2004 *An Improved Demosaicing Algorithm* Graphicon-Moscow, Russia, September 2004.

[26] Yuan B., Yan H.M., Cao X.Q. 2009 *A new subdivision method for grating-based displacement sensor using imaging array* Opt. Lasers Eng. **47** 90–95.